

# Water self-dissociation under the microscope: the $K_w$ in confinement

Solana Di Pino<sup>a,b</sup>, Yamila A. Perez Sirkin<sup>a</sup>, Uriel N. Morzan<sup>c</sup>, Verónica M. Sánchez<sup>b</sup>, Ali Hassanali<sup>c,1</sup>, Damian A. Scherlis<sup>a,1</sup>,

**a.** Departamento de Química Inorgánica, Analítica y Química Física/INQUIMAE, Facultad de Ciencias Exactas y Naturales, Universidad de Buenos Aires, Buenos Aires, Argentina

**b.** Centro de Simulación Computacional para Aplicaciones Tecnológicas, Polo Científico y Tecnológico, CONICET, Buenos Aires, Argentina

**c.** International Centre for Theoretical Physics, Trieste, Italy

<sup>1</sup> E-mail: ahassana@ictp.it or damian@qi.fcen.uba.ar.

## Significance

Water reactivity in confinement rules chemistry in aerosols, membranes, protein pockets and nanopores. Confinement can accelerate chemical kinetics by orders of magnitude, offering a venue to novel synthetic strategies. However, our understanding of the reactivity of nanoconfined water is poor, and the ways in which confinement affects its dissociation remain elusive. This work provides a comprehensive explanation of what determines the equilibrium constant  $K_w$ , and how it changes in different environments. Against previous hypothesis and speculations, it shows that the dissociation free-energy is invariant with respect to size, down to the nanometer scale. This implies that, unless system dimensions become comparable to the molecular diameter, interfacial effects, rather than confinement itself, are the main actors influencing water reactivity in nanospaces.

## Abstract

Nanoconfinement has been shown to drastically affect the physical properties of water. Its effects on reactivity and dissociation, however, remain controversial, despite their importance to understand aqueous chemistry at interfaces, pores, aerosols or protein cavities, and the growing evidence indicating the acceleration of chemical kinetics in confined environments. The dissociation constant  $K_w$  in nanospaces has been assessed from experiments and simulations in a few specific cases, leading to dissimilar conclusions. Here, using carefully designed ab-initio simulations and data-science tools, we demonstrate, challenging current misconceptions, that the energetics of bulk water dissociation remains unchanged to surprisingly small length-scales including clusters of only a dozen water molecules. This is rooted in the fact that most of the free-energy involved in water autoionization comes from breaking the O-H covalent bond, which has a comparable barrier in the bulk liquid or in droplets of nanometer size. The subsequent separation of the hydroxide and hydronium species contributes a marginal fraction of the total free-energy, for which reason it turns out that confinement exerts little control on this process. The present work provides a definitive and fundamental description of the mechanism and thermodynamics of water dissociation at different scales with broader implications on water's self-ionization at the air-liquid interface and on chemical reactivity under nanoconfinement.

---

## Introduction

Confinement deeply affects the physical chemistry of water. In cavities or pores of a few nanometers, its freezing point can drop as much as 50°C [24, 38, 49], while other dynamic and thermodynamic properties such as diffusivity [6, 20, 34, 51, 60], dielectric constant [11, 36, 37, 48], melting enthalpy [17, 26], or thermal expansion [27, 62], experience significant changes. Remarkable progress has been made in the investigation of water at the nanoscale regime: spectroscopic and calorimetric techniques [3, 6, 20, 26, 34, 35, 35, 47, 49, 60], hand in hand with molecular simulations [8, 16, 23, 36, 37, 51, 55, 58, 64], have been ingeniously applied to probe and characterize the structure, dynamics, and phase transitions of water in nanometric domains.

Notwithstanding these achievements, the role of confinement on chemical reactivity is barely understood, mostly because of the complexity associated with the determination of equilibrium and kinetic constants in these conditions. In particular, the dissociation of water confined in porous media, tiny aerosols, biomolecules, membranes, and other nanospaces, represents a fundamental problem of extreme relevance for experimentalists, which remains unsettled. Studies in nanodroplets, reverse micelles, and cavities within supramolecular assemblies, all strongly suggest that chemical kinetics is substantially affected with respect to the bulk phase, producing accelerations of up to 6 orders of magnitude in some cases [9, 12, 19, 32, 61, 63]. This has prompted researchers to focus on confined chemistry in the search of alternative routes for chemical synthesis [9, 12, 19, 63], to elucidate chemical transformation in the atmosphere [65], or to explain enzymatic catalysis in living organisms [28, 54]. Whereas the mechanisms behind these increased rates are still a matter of debate, the main causes that have been postulated include the over-concentration of reagents, extreme pH changes, or interfacial and entropic effects. Among the latter, the equilibrium constants of products, reagents, and solvent, all become critical [46]. Understanding how water dissociation is affected in nanoenvironments together with its role in aqueous reactivity is thus a key pending question.

Speculations based on indirect experimental evidence and theoretical conceptions have been made on a possible enhancement of the aqueous acidity in nanocavities [43]. In a very recent NMR study, on the other hand, a single H<sub>2</sub>O molecule confined in the pocket of a C<sub>60</sub> derivative was shown to be less acidic than bulk water [21]. In any case, the effect of pore radius and of the nature of the interface on the dissociation constant of water continues to be a basic question still unanswered from a general perspective. Hence, simulations become essential and have in fact contributed a number of clues that shed light on this matter.

First-principles simulations proved useful to calculate the pK<sub>w</sub> in bulk [52, 57], and were also applied to investigate the autoionization in confinement in various settings, from the interlayer spaces of minerals to carbon nanotubes [33, 40, 50]. In particular, Muñoz-Santiburcio and Marx computed the self-dissociation constant in slit pores of 1 nm delimited by FeS layers, at high temperature and pressure [40]. They claimed that the free-energy barrier to dissociation ( $\Delta G_d$ ) experienced a reduction of more than 15%, explained in terms of an increase in the dielectric constant arising from confinement.

In the present study, we use state-of-the-art ab-initio molecular simulations in combination with an appropriate sampling coordinate to track how the water dissociation barrier is affected by system size, hence providing a general answer to the puzzle on whether and by how much the self-dissociation of water changes under confinement. We formulate and respond the question of how big the aqueous domain must be to preserve the energetics and the mechanism of bulk water dissociation. The answer is surprising: an aqueous cluster of just a dozen molecules exhibits a dissociative free-energy profile that cannot be distinguished from the one corresponding to the bulk

phase. Size effects can only be seen in an aggregate that has half this number of molecules, where solvation of the hydronium and hydroxide ions are severely hindered. Our work rationalizes this outcome with the help of data-science tools, and manages to reconcile previous, apparently contradictory findings, offering a comprehensive picture of water dissociation at the nanoscale. Beyond its obvious impact on chemistry under confinement, the results of our simulations have broader implications on how the  $pK_w$  changes near hydrophobic interfaces such as the surface of water or aqueous solutions.

## Results and discussion

### Dissociation free-energy of nanoconfined water

The dissociation free energy of water in the bulk phase was first computed from ab-initio molecular simulations in the late 90's by Trout and Parrinello [57]. These authors adopted the O-H distance of the dissociating bond as the reaction coordinate. While this constraint proved to be appropriate to induce bond breaking and to form the ion pair, when the O-H separation exceeds a certain length, it can not prevent the recombination of the hydroxide with a different proton through Grotthuss diffusion [52]. Thus, the application of this scheme seems to be unable to produce a well separated  $\text{OH}^-$ - $\text{H}_3\text{O}^+$  pair. Shortly after, Sprik proposed the proton coordination  $n_H$  as an alternative reaction coordinate that, by avoiding recombination, may facilitate the separation of the ions [52]. This variable, implemented in some of the studies cited above [33, 40, 50], counts the number of protons surrounding a given oxygen atom. Each H atom contributes to  $n_H$  with a quantity that varies continuously between 0 and 1, depending on the O-H distance (see SI Appendix). Thus, the proton coordination assumes fractionary values and can be used to introduce a bias potential that enforces dissociation in a particular  $\text{H}_2\text{O}$  molecule as  $n_H$  changes from 2 to 1.

Using this strategy, we calculated the dissociation free energy for isolated water clusters of 6, 12, and 20 molecules of  $\text{H}_2\text{O}$ . The results are presented in Figure 1, together with the curve corresponding to bulk water. Something remarkably surprising happens: the free energy profile for the aggregate of 12 molecules, with an average diameter not larger than 1 nm, does not differ, within the error of the method, from the one obtained for the system of 20 molecules, and the two of them are in turn indistinguishable from the curve corresponding to the bulk phase. Since the dissociation of water creates two ions, it can be expected that their solvation energy would be strongly modulated by the size of the hydrogen bond network. Instead, a change in the barrier is only observed for the smallest system consisting of 6 molecules, where  $\Delta G_d$  increases by nearly 30%, corresponding to a drop of 3 orders of magnitude in  $K_w$ .

This unanticipated outcome, i.e., the insensitivity of water dissociation with respect to system size, is consistent with the data from ab-initio simulations presented by Liu and coworkers, showing that in 1.5 nm slit pores of layered neutral clay models,  $K_w$  was essentially the same as in bulk water [33]. These authors reported that the acidity was increased in the presence of interstitial  $\text{Mg}^{2+}$  cations, while remaining almost unaltered in a neutral environment, attributing to the charge, and not the confinement itself, the rise in  $K_w$ . On the other hand, this seems to be at odds with the more recent work from Marx's group [40], ascribing to bidimensional confinement in slit pores of 1 nm, an enhancement of  $55\times$  in the self-dissociation constant  $K_w$ . This disagreement between these two studies is rather puzzling, given that they share the same methodology, based on DFT Car-Parrinello molecular dynamics and the proton coordination  $n_H$  as the reaction coordinate.

A careful analysis of these reports, however, discloses the origin of this apparent contradiction. In the *NVT* simulations by Muñoz-Santiburcio and Marx, the density,

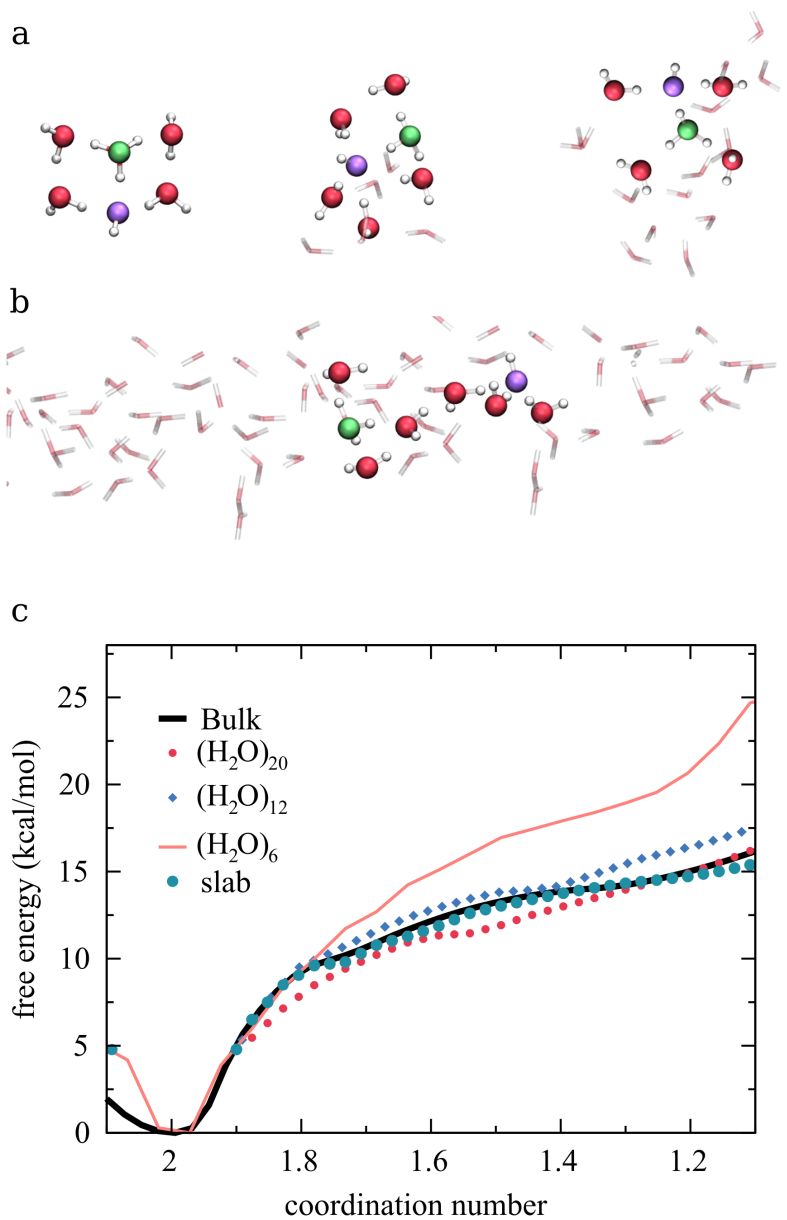


**Figure 1.** Free-energy profiles for various water model systems. **a:** Snapshots of the (H<sub>2</sub>O)<sub>6</sub>, (H<sub>2</sub>O)<sub>12</sub>, and (H<sub>2</sub>O)<sub>20</sub> clusters illustrating the product (dissociated) state. Oxygen atoms belonging to the OH<sup>-</sup> and H<sub>3</sub>O<sup>+</sup> ions are shown in blue, including the hydrogen-bonded molecules in a balls-and-sticks depiction. **b:** Periodic slab water model of width 1 nm. **c:** Free energy profiles computed for the dissociation of water in the bulk phase, and for the model systems represented above. The coordination number alludes to the proton coordination of the oxygen atom in the donor water molecule.

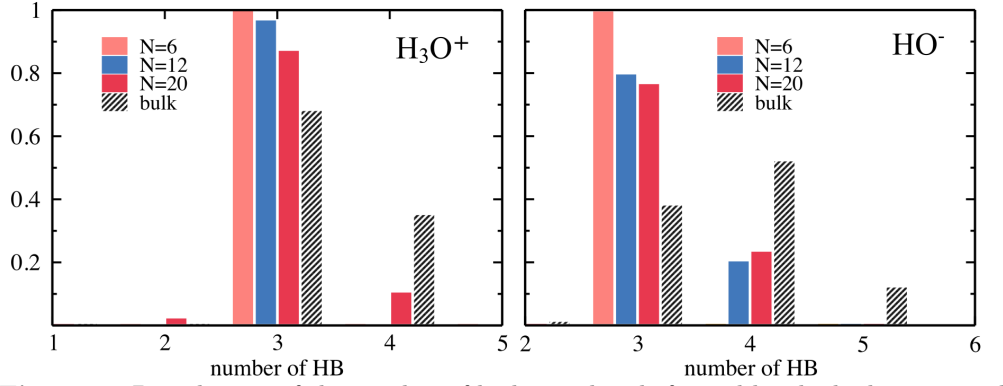


**Figure 2.** Distribution of the number of hydrogen bonds formed by the hydronium and the hydroxide ions in the clusters and in the bulk phase.

and not the pressure, was the thermodynamic variable under control. In particular, the number of water molecules  $N$  filling the pore was not equilibrated with a reservoir at the desired pressure, but was fixed to yield a target density  $\rho$ , with  $N = \rho \times V_{eff}$ . However, the accessible volume  $V_{eff}$  is not an unambiguously defined quantity: it suffers from the arbitrariness associated with the atomic radii. In spite of this,  $V_{eff}$  needs to be prudently chosen because it has a direct impact on the effective  $\rho$ . In ref. [40], the criterion to define the accessible space was fairly conservative, resulting in an overestimation of  $V_{eff}$  by at least 30% [1]. As a consequence, the fluid in the pore was overcompressed with respect to the target pressure, producing the observed enhancement in  $K_w$  that was attributed to a confinement effect—the dissociation constant of water is known to grow as a function of pressure [4]. In fact, the simulations recovered the bulk value of the  $\text{pK}_w$  when  $\rho$  was reduced by 35% (Figure 3 in ref. [40]). In the study by Liu et al., instead, the number of water molecules included in the supercell was adopted from classical grand-canonical molecular dynamics, where the density had reached its equilibrium value at 1 bar [33]. In that work, the dissociation constant inside the neutral nanopore showed no significant differences with respect to the bulk phase.

To corroborate this, we applied the same protocol to compute the water dissociation free-energy in an extended slab of 1 nm width in the vacuum. This slab consisted of 32  $\text{H}_2\text{O}$  molecules contained in a supercell of lateral dimensions  $14.69 \times 14.69 \text{ \AA}^2$ , approximately the same as those used in ref. [40]. These simulations recreate the conditions of bidimensional confinement, avoiding any compression effects—since the water structure can equilibrate with the gas phase—and suppressing the interactions with the pore walls. In this way, the emerging free-energy profile expresses the sole effect of 2D confinement. This profile is depicted in Figure 1, where it can be seen that  $\Delta G_d$  turns out to be—within the error of our method—not different from the one corresponding to the bulk liquid.

The question that naturally arises is: what is the rationale for the observed trend in the  $\text{pK}_w$ ? A simple explanation can be given in terms of the hydrogen bond structure. The dissociation free-energy is determined by the thermodynamic stability of the products, hydronium and hydroxide, which will in turn depend on the ability of the hydrogen bond network to solvate these ions. Figure 2 summarizes the information regarding the number of hydrogen bonds in the clusters and in the bulk, showing that the  $\text{OH}^-$  anion loses one hydrogen bond in the smallest cluster with respect to the rest of the environments. In the bulk phase, the hydroxide accepts 4 strong hydrogen bonds and donates a weak one [2]. A detailed analysis of the hydrogen bond network, as the

**Table 1.** Average distribution of hydrogen bonds for the hydroxide and hydronium species.

		donates	accepts
BULK	H <sub>3</sub> O <sup>+</sup>	3	1
	OH <sup>-</sup>	1	3-4
N=20	H <sub>3</sub> O <sup>+</sup>	3	0
	OH <sup>-</sup>	0	3-4
N=12	H <sub>3</sub> O <sup>+</sup>	3	0
	OH <sup>-</sup>	0	3-4
N=6	H <sub>3</sub> O <sup>+</sup>	3	0
	OH <sup>-</sup>	0	3
SLAB	H <sub>3</sub> O <sup>+</sup>	3	0
	OH <sup>-</sup>	0	3-4

one provided in Table 1, reveals that in the 6 molecules aggregate, the hydroxide accepts only 3 hydrogen bonds, while it accepts up to 4 in all the other systems. This missing bond appears to be the reason for its destabilization and the rise in  $K_w$  when  $N=6$ . Moreover, the hydronium ion donates 3 strong and accepts one weak hydrogen bond in the bulk. In the clusters the latter interaction is lost, however this does not appear to significantly affect the thermodynamics of dissociation. The fact that the oxygen of the hydronium is rather hydrophobic [2] can explain why placing it in a small cluster does not incur a large energetic cost.

### What it takes to drive the ions apart

Up to now, the rationalization of the dissociation free energy has namely involved the energetic contribution of breaking the covalent bond and the reorganization of hydrogen bonding. Nevertheless, once the ions are formed, they must separate away from each other creating solvent screened entities. The underlying mechanism by which this happens and the corresponding thermodynamics has been a topic of lively discussion in the literature. First-principles simulations by Geissler and co-authors have shown that the stabilization of the products in the autoionization of water requires the ions to be separated by at least three bonds; in that situation, a fluctuation that interrupts the “hydrogen bond wire” facilitates the diffusion of the proton through the Grotthuss mechanism, thus leading to the effective separation of the hydroxide and hydronium species [13]. More recent work by Hassanali and co-workers has shown the hydrogen bond wire undergoes collective compressions which are essential for the proton transfer and hydronium-hydroxide separation [22]. Using machine-learning approaches, van Erp and co-workers proposed that besides the wire compression, factors such as the alignment of the hydrogen bond wire and the extent of tetrahedrality of the water molecules also play important roles [39].

In the clusters, their own size restrains the maximum separation that the ions can attain. The average hydroxide-hydronium distances ( $d_{12}$ ) fluctuate around 2.5-3.5 Å during the molecular dynamics sampling in the different aggregates (SI Appendix), reflecting that these ionic species are rarely separated by more than one hydrogen bond. This behavior is also observed in the bulk: the trajectories show that even for the lowest values of  $n_H$ , the hydroxide and the hydronium tend to reside not further than two bonds apart, and that they may even be in contact most of the time. The dimensions of the supercell are in principle large enough to enable a separation between the counterions of up to five hydrogen bonds, or  $d_{12} \sim 10$  Å. The fact that distances beyond 4 Å are seldom explored suggests that the use of  $n_H$  as the reaction coordinate may not

be effective to create fully solvated and decorrelated hydronium and hydroxide ions. It is thus reasonable to wonder whether our computations are missing an additional contribution to the free energy associated with a further delocalization of the ions that may account for a difference between the bulk and the confined systems.

To enforce a full separation of the ions, a new reaction coordinate can be defined composed of the proton coordination of two different, distant oxygen atoms,  $n_H(1)$  and  $n_H(2)$ . By setting the reaction coordinate as the difference between these two,  $\xi(\Delta n_H) = n_H(2) - n_H(1)$ , and sampling the phase space from  $\xi=0$  to  $\xi=2$ , it is possible to drive a proton from a given water molecule (containing oxygen 1) to another chosen molecule (containing oxygen 2) lying far away, thus producing a well separated  $\text{OH}^-$ - $\text{H}_3\text{O}^+$  pair. The distance between these two water molecules may slightly vary during the process, however, their diffusion is negligible within the elapsed time.

Figure 3a presents the free-energy resulting from this scheme (blue curve) with oxygens 1 and 2 initially separated by  $\sim 8$  Å. In addition, the profile obtained earlier is also shown in red on the right panel for easy comparison. To interpret the free-energy curve in blue, it is first important to identify the reaction endpoint. This can be associated with a value of  $n_H$  equal to the coordination number corresponding to aqueous  $\text{OH}^-$  in the bulk phase, which, according to our simulations, turns out to be around 1.35 [50]. Figure 3c shows that this coordinate effectively draws the hydroxide and hydronium species apart over the target distance. In Figure 3d,  $n_H(1)$  and  $n_H(2)$  are plotted as a function of the global reaction coordinate  $\xi$ . In particular,  $n_H(1)$  reaches a value of 1.35 when  $\xi \sim 1.4$ , implying that at this point the reaction is complete. In this region the free energy profile comes to a plateau at an energy that corresponds almost exactly to the value of  $\Delta G_d$  resulting from the sampling based on the proton coordination of a single oxygen, shown in the same graph. All in all the comparison of both curves in Figures 3a and 3b provides two fundamental insights: (i) the spatial decorrelation of the nascent  $\text{H}_3\text{O}^+$  and  $\text{OH}^-$  ions contributes a negligible fraction of the overall free-energy, meaning that the barrier is dominated by the dissociation step involving breaking the covalent bond that produces the contact ion-pair; (ii) a complete separation of the ions, attainable through the global reaction coordinate  $\xi$ , is needed to reach a (metastable) flat region in the free-energy profile, that is not observed with the adoption of a reaction coordinate based on a single oxygen atom.

Further examination of Figure 3d reveals that a gradual protonation of the acceptor  $\text{H}_2\text{O}$ , effected at the expense of the partial dissociation of neighboring molecules, precedes the deprotonation of the donor. The coordination number of the latter,  $n_H(1)$ , remains approximately constant while the system climbs up the free-energy surface, up to  $\xi \sim 1.2$ , when it suddenly drops to its endpoint value. Concurrently with this last event, the average separation between the hydroxide and the hydronium species increases by several angstroms. The fluctuations that occur within the hydrogen bond network to facilitate the sequence of events leading to the separation of the contact-ion pair, illustrated in Figure 4a, have been the subject of several previous studies [13,22].

The contribution of the hydrogen bond network beyond the first solvation shell to the self-dissociation of water can be interpreted in terms of the dynamical correlation functions  $C(r)$  based on the fluctuations of the atomic positions. These correlations quantify the entanglement between the dynamics of the incipient ions and that of the water molecules situated at a distance  $r$  (see SI Appendix). Figures 4b and 4c evidence a dynamics of the acceptor and donor water molecules primarily correlated with or influenced by their first solvation shell. As the global coordinate evolves towards the formation of the ions, the relative influence of solvation beyond the first neighbors decreases substantially, reaching a minimum at  $\xi \sim 0.6$ . At this point, the dynamics of the nascent ions is only coupled to their first solvation layer, independent of the fluctuations taking place further away. For larger values of  $\xi$  until completion of the

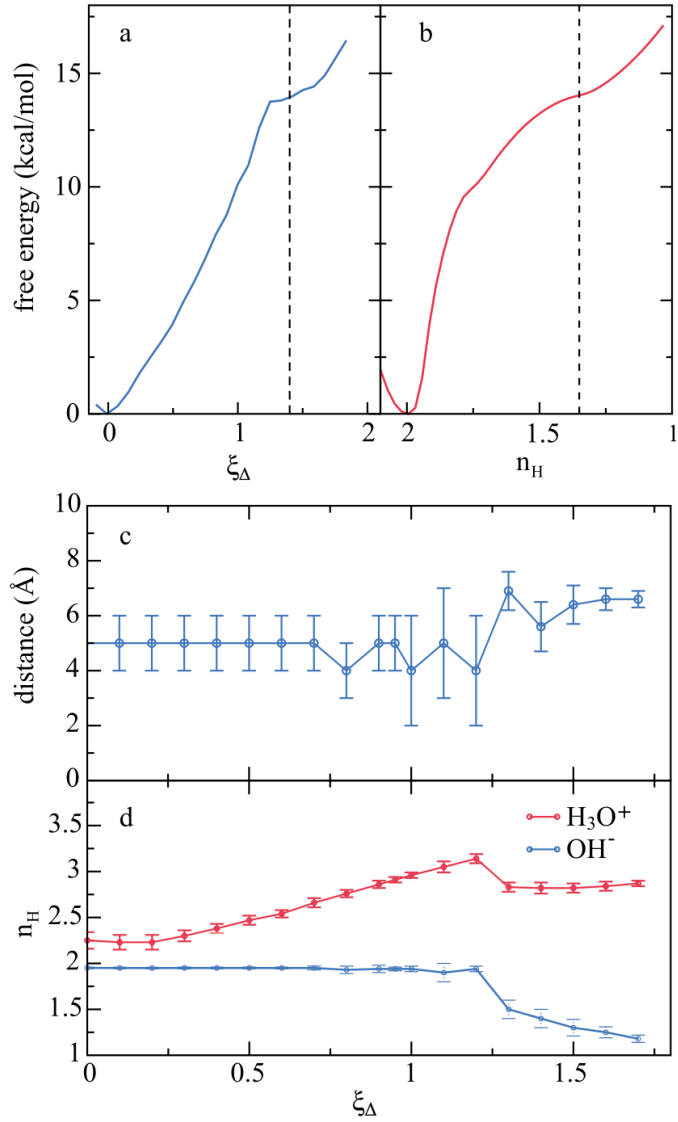


**Figure 3.** Evolution along the reaction coordinate. **a** and **b**: Free energy profiles for the dissociation of water in the bulk phase, computed with the single-oxygen reaction coordinate  $n_H$  (red curve) and with the global reaction coordinate  $\xi(\Delta n_H)$  (blue curve). The dashed vertical line marks the reaction endpoint for both coordinates. **c**: Average separation  $d_{12}$  between the hydroxide and hydronium species as a function of the global reaction coordinate  $\xi(\Delta n_H)$ . This separation is defined and computed as the distance between the oxygen atoms exhibiting the maximum and minimum proton coordinations. At the early stages of the reaction, when the proton is still bound to the parent water molecule, the fluctuations of the hydrogen-bond network randomly switch the identity of the minimum coordination oxygen atom, and therefore the value of  $d_{12}$  turns out to be an average of all O-O distances in the supercell ( $\sim 5$  Å). It is only when the reaction is close to completion that  $d_{12}$  achieves the targeted value. **d**: Proton coordination number of the oxygen atoms in the donor (blue) and acceptor (red) water molecules, as a function of the reaction coordinate.



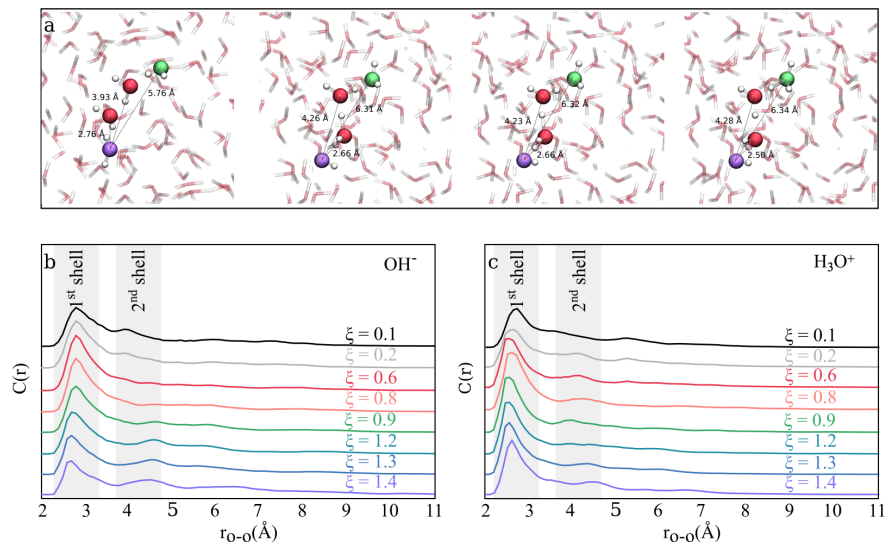


**Figure 4.** Characterization of the self-dissociation mechanism. **a:** Snapshots selected from umbrella sampling trajectories in the bulk phase, illustrating the dissociation mechanism. Break of the O-H bond leaves a contact ion pair, until a proper alignment of the water wire (depicted in indigo) allows for a barrierless diffusion of the proton via the Grotthuss mechanism. **b:** Dynamical radial correlation functions  $C(r)$ , quantifying the coupling between the dynamics of the nascent  $\text{OH}^-$  ion and the water molecules placed at  $r$ , computed for different values of the global reaction coordinate  $\xi$ . **c:** Same as **b** for the  $\text{H}_3\text{O}^+$  ion.

ionization, the second solvation shell slowly regains influence over the ion dynamics (clearly illustrated by the relative dynamical correlation functions presented in the SI Appendix).

The increasing decoupling between the ions and their second solvation shells during the initial stages of the self-dissociation process attest that the dynamics of the reactants will be largely unaltered by perturbations beyond the closest neighbors. This fact explains the insensitivity of the free energy profile to size reduction beyond the first shell, reinforcing the mechanism proposed above: the formation of the contact ion pair takes most of the free-energy rise, eventually followed by a barrierless proton diffusion propitiated by a favorable alignment of the hydrogen bond network, manifest in the last part of the mechanism ( $\xi \sim 1.3$ ) where  $C(r)$  presents some structure beyond the first neighbors.

## Concluding remarks

Through the application of first-principles biased molecular dynamics simulations combined with an innovative reaction coordinate, the present study conclusively establishes that the dissociation free-energy of water is determined by the initial break of the O-H covalent bond. The subsequent separation of the formed ions, via Grotthuss diffusion, is energetically costless. As a consequence, the  $\text{pK}_w$  turns out to be practically invariant with respect to system dimensions, providing that they do not interfere with the solvation of the products. A sizeable drop in  $K_w$  is only seen when the first solvation shell of the ions is not intact, and in particular when the acceptor role of  $\text{OH}^-$  is affected. In clusters, this occurs at some point between  $N=6$  and  $N=12$ . It is suggestive that the change in  $K_w$  with respect to size stabilizes when the droplet

---

approaches the length-scale for which hydrogen-bond networks develop, namely, the water hexamer [42,44]. Thus, dissociation free-energy profiles in nanoscopic aggregates or in a 2D slab of 1 nm width reproduce the behavior corresponding to the bulk phase, with differences only manifesting at subnanometer confinement.

In real chemical systems, it is often not possible to consider size effects separately from interfacial interactions. The presence of charges or polar surface groups, able to establish specific interactions with H<sub>2</sub>O and with its ions, will have a disrupting incidence on aqueous reactivity. Many examples can be found in the literature discussing the acceleration or inhibition of reactivity under confinement [10,19,32,46,63]. Leaving aside physical effects as those examined in refs. [46] and [10], the interactions with the interface appear to be the main factor controlling mechanisms and energetic barriers. Indeed, the present results suggest that confinement alone will not affect the chemistry of water unless system dimensions become comparable to the molecular size. A broader implication of this finding is that water’s self-ionization constant at the hydrophobic air-liquid interface will remain unchanged, warranting further study.

## Methods

Ab-initio simulations were based on density functional theory (DFT) and Car-Parrinello molecular dynamics. Computations were performed using the Quantum-Espresso code [14], which relies on plane-wave basis sets and pseudopotentials to expand the electronic states. Free-energy profiles were obtained from Umbrella sampling as a function of proton coordination. Details on the DFT calculations, molecular dynamics, the thermodynamic integration, and the dynamical correlation functions, are provided in the *SI Appendix*.

## Acknowledgments

We are grateful to Mariano Gonzalez Lebrero for useful discussions. This work has been funded by the Agencia Nacional de Promoción Científica y Tecnológica de Argentina (PICT 2015-2761 and PICT 2016-3167).

## Supporting Information

### Methodology

Simulations were performed using the Quantum-Espresso code, which is an efficient, open-source implementation of density functional theory (DFT) in periodic boundary conditions [14,15]. The standard package was modified to carry out free-energy calculations based on the proton coordination number. Energy and forces were computed with the BLYP exchange-correlation functional [5,31] including Grimme’s Van der Waals corrections [18] and combined with Vanderbilt ultrasoft pseudopotentials [59]. The Kohn-Sham orbitals and the charge density were expanded in plane-waves basis sets with kinetic energy cutoffs of 20 and 160 Ry, respectively. Car-Parrinello molecular dynamics simulations [7] were performed using an effective electron mass of 400 a.u., coupled to a Nosé-Hoover thermostat at 300 K and a time step of 0.145 fs. Reciprocal space sampling was restricted to the  $\Gamma$ -point.

Dissociation free-energies were obtained from Car-Parrinello molecular dynamics simulations combined with the umbrella sampling scheme [56], with a reaction

coordinate defined in terms of the proton coordination  $n_H$  introduced by Sprik [53]:

$$n_H(j) = \sum_i^{N_H} \frac{1}{\exp[\kappa(r_i - r_c)] + 1} \quad (1)$$

where  $N_H$  is the number of H atoms in the system,  $r_i$  the distance from oxygen atom  $j$  to proton  $i$ , and the parameters  $\kappa$  and  $r_c$  are chosen to produce a continuous coordination index [53]. All protons lying closer than  $r_c - \kappa^{-1}$  add one to this sum, those further than  $r_c + \kappa^{-1}$  are excluded, and those protons located in between contribute with a fractional weight, thus providing a continuous measure of the number of H atoms bound to the oxygen  $j$ , that turns out to be a suitable reaction coordinate. For  $\kappa$  and  $r_c$  we employed the values of  $10 \text{ \AA}^{-1}$  and  $1.38 \text{ \AA}$  respectively, as proposed in reference [53].

The thermodynamic integration was carried out according to the Umbrella sampling protocol, in which the total energy was modified by adding a harmonic potential of the form

$$V_u(t) = \frac{1}{2}k_u(\chi(t) - \chi^0)^2$$

where  $\chi(t)$  can be either the instantaneous proton coordination introduced in equation (1), or the difference in proton coordinations of two oxygen atoms,  $\xi = n_H(2) - n_H(1)$ . On the other hand,  $\chi^0$ , the reaction coordinate, was kept constant throughout the dynamics. To compute a single free-energy profile, around 20 molecular dynamics trajectories were performed, each one for a different value of  $\chi^0$ . This parameter was varied between 1.0 and 2.0 in the case of the proton coordination reaction coordinate, and between 0 and 2.0 when the compounded coordinate  $\xi$  was used. The force constant  $k_u$  was adjusted to achieve an appropriate sampling. Its optimal value arises from a compromise between the need to constrain the dynamics around the desired reaction coordinate, and the convenience to explore the largest possible portion of the phase space to minimize the number of windows. A histogram was produced for each value of  $\chi^0$ , reflecting the (logarithmic) probability distribution. For each window associated with a certain value of  $\chi^0$ , initial configurations were extracted from thermalized classical molecular dynamics, and thereafter, Car-Parrinello trajectories were run for 17 ps, of which the initial 5.8 ps were discarded. These time-lengths were checked to provide converged free-energy curves. Every histogram was then weighted by the exponential factor  $\exp[-\frac{1}{2}k_u(\chi - \chi^0)^2]$ , to extract a piece of curve representing the free energy around  $\chi^0$ . Finally, the free energy profile was constructed by matching these pieces corresponding to adjacent values of  $\chi^0$ , according to the Weighted Histogram Analysis Method [25, 29].

## Model systems

Simulations of water clusters and of the bulk model of 32  $\text{H}_2\text{O}$  molecules were conducted in cubic cells of lattice parameters  $21.17 \text{ \AA}$  and  $9.86 \text{ \AA}$ , respectively. Test calculations showed that the results were converged with respect to size. In particular, the curve corresponding to a model of 32 water molecules did not exhibit any significant difference from that of 64 molecules. The bulk dissociation profiles obtained from those trajectories ending up in a separation of a couple of bonds between the hydronium and the hydroxide, proved to be indistinguishable from those profiles derived from trajectories where the ions remained in contact. For the slab, a supercell of dimensions  $14.69 \text{ \AA} \times 14.69 \text{ \AA} \times 16.73 \text{ \AA}$  was adopted. Such a slab model in the vacuum may be thermodynamically unfavored with respect to a cluster of that size in the same supercell; however, the barrier between both configurations is such that the slab remains stable for the whole trajectories.

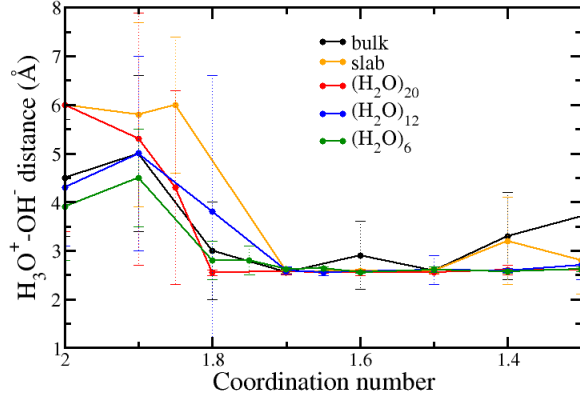


**Figure 5.** Average separation between the ions as a function of the proton coordination reaction coordinate.

### Hydroxide-hydronium separation

Figure S1 illustrates the average separation between the ions as a function of the proton coordination reaction coordinate. Since the  $\text{OH}^-$  and  $\text{H}_3\text{O}^+$  ions are labelled in terms of the oxygen atoms bearing the minimum and maximum proton coordination respectively, in the “reactive state” ( $n_H \sim 2$ ) when ionization is still incipient, all water molecules are equivalent and the computed distance is just an average of all O-O lengths in the unit cell. This explains the larger distances for coordination numbers larger than 1.8.

### Dynamical correlation functions

The use of dynamical correlations based on the fluctuations of the atomic positions is a common practice in the literature (see for example refs. [30, 41, 45]). Here we define the dynamical radial correlation function  $C^i(r)$  associated with the nascent ion  $i$  ( $i = \text{OH}^-$  or  $\text{H}_3\text{O}^+$ ) as

$$C^i(r) = C_c^i(r) + C_{\text{nc}}^i(r) \quad (2)$$

where  $C_c^i(r)$  and  $C_{\text{nc}}^i(r)$  are the collinear and non-collinear contributions, respectively. The first one is a Pearson correlation,

$$C_c^i(r) = \left\langle \frac{1}{n_i(r)} \sum_j^{n_i(r)} \frac{\delta_i \cdot \delta_j}{\sqrt{\langle \delta_i \rangle^2 \langle \delta_j \rangle^2}} \right\rangle, \quad (3)$$

whereas the second one accounts for the directionality of the fluctuations, and has been adapted from ref. [30]:

$$C_{\text{nc}}^i(r) = \left\langle \frac{1}{n_i(r)} \sum_j^{n_i(r)} \frac{\sum_k^3 \sum_{m \neq k} \delta_i \hat{x}_k \delta_j \hat{x}_m}{(\sum_{k'}^3 \sum_{m' \neq k'} \langle \delta_i \rangle \hat{x}_{k'} \langle \delta_i \rangle \hat{x}_{m'}) (\sum_{k''}^3 \sum_{m'' \neq k''} \langle \delta_j \rangle \hat{x}_{k''} \langle \delta_j \rangle \hat{x}_{m''})} \right\rangle. \quad (4)$$

In the equations above,  $\delta_i = \mathbf{r}_i - \langle \mathbf{r}_i \rangle$ , and  $n_i(r)$  is the number of molecules within a distance  $r$  and  $r + dr$  from molecule  $i$ .  $C^i(r)$  is a measure of the entanglement between the dynamics of the nascent ion  $i$  and the atoms placed between  $r$  and  $r + dr$  from it.

The  $C^i(r)$  curves were computed for every umbrella sampling window performed on the  $\xi$  reaction coordinate. In order to interpret the  $\xi$ -dependence of the radial correlation profiles, the  $C^i(r)$  distributions were normalized by their total area and a

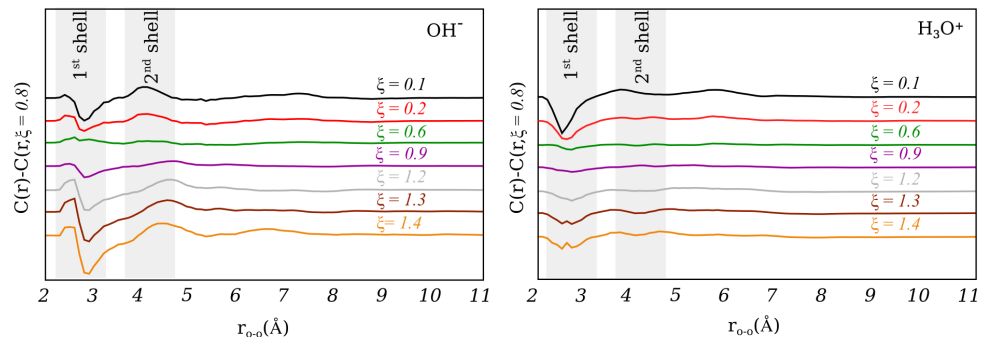


**Figure 6.** Difference between  $C(r)$  for a given value of  $\xi$  and that corresponding to  $\xi = 0.8$  (both presented in Figure 4 of the main text).

mean-filter procedure was applied. For each  $r$ , the mean-filtered  $C^i(r)$  was computed as the average between  $C^i(r)$ ,  $C^i(r - dr)$ , and  $C^i(r + dr)$ .

Figure S2 displays the difference between  $C(r)$  for a given value of  $\xi$  and that corresponding to  $\xi = 0.8$  (both presented in Figure 4 of main text). This graph allows for a finer appreciation of the differences in dynamical correlations as a function of the reaction coordinate.

## References

1. In ref. 40 the accessible volume was defined in terms of the density profile along  $z$ , the direction normal to the confining surfaces (see Fig. 1 in the SI of ref. 24). In particular, the authors chose the region between  $z \approx -4$  and  $z \approx +4$  Å as the accessible volume. At these points the density has far vanished, which means that water molecules are practically excluded from the region next to these limits. At the nanoscale, less arbitrary, physically meaningful definitions of  $V_{eff}$  can be constructed from the numerical integration of the density profile [see for instance *J. Phys. Chem. Lett.* (2019) 10, 6287]. With such a criterion, the accessible space would not extend beyond  $z \approx -3$  and  $z \approx +3$  Å, implying that the effective density in the simulations of ref. 24 exceeded the targeted  $\rho$  by no less than 30 %.
2. N. Agmon, H. J. Bakker, R. K. Campen, R. H. Henchman, P. Pohl, S. Roke, M. Thämer, and A. Hassanali. Protons and hydroxide ions in aqueous systems. *Chem. Rev.*, 116(13):7642–7672, 2016.
3. K. V. Agrawal, S. Shimizu, L. W. Drahushuk, D. Kilcoyne, and M. S. Strano. Observation of extreme phase transition temperatures of water confined inside isolated carbon nanotubes. *Nat. Nanotechnol.*, 12(3):267, 2017.
4. A. V. Bandura and S. N. Lvova. The ionization constant of water over wide ranges of temperature and density. *J. Phys. Chem. Ref. Data*, 35:15–30, 2006.
5. A. D. Becke. *Phys. Rev. B*, 38:3098, 1988.
6. I. M. Briman, D. Rébiscoul, O. Diat, J.-M. Zanotti, P. Jollivet, P. Barboux, and S. Gin. Impact of pore size and pore surface composition on the dynamics of confined water in highly ordered porous silica. *J. Phys. Chem. C*, 116(12):7021–7028, 2012.

7. R. Car and M. Parrinello. Unified approach for molecular dynamics and density-functional theory. *Phys. Rev. B*, 55:2471–2474, 1985.
8. E. de la Llave, V. Molinero, and D. A. Scherlis. Role of confinement and surface affinity on filling mechanisms and sorption hysteresis of water in nanopores. *J. Phys. Chem. C*, 116(2):1833–1840, 2012.
9. T. Dwars, E. Paetzold, and G. Oehme. Reactions in micellar systems. *Angew. Chem. Int. Ed.*, 44:7174–7199, 2005.
10. A. Fallah-Araghi, K. Meguellati, J.-C. Baret, A. E. Harrak, T. Mangeat, M. Karplus, S. Ladame, C. M. Marques, and A. D. Griffiths. Enhanced chemical synthesis at soft interfaces: A universal reaction-adsorption mechanism in microcompartments. *Phys. Rev. Lett.*, 112:028301, 2014.
11. L. Fumagalli, A. Esfandiar, R. Fabregas, S. Hu, P. Ares, A. Janardanan, Q. Yang, B. Radha, T. Taniguchi, K. Watanabe, G. Gomila, K. S. Novoselov, and A. K. Geim. Anomalously low dielectric constant of confined water. *Science*, 360(6395):1339–1342, 2018.
12. A. Gallo, A. S. F. Farinha, M. Dinis, A.-H. Emwas, A. Santana, R. J. Nielsen, W. A. Goddard, and H. Mishra. The chemical reactions in electrosprays of water do not always correspond to those at the pristine air-water interface. *Chem. Sci.*, 10:2566–2577, 2019.
13. P. L. Geissler, C. Dellago, D. Chandler, J. Hutter, and M. Parrinello. Autoionization in liquid water. *Science*, 291:2121–2124, 2001.
14. P. Giannozzi, O. Andreussi, T. Brumme, O. Bunau, M. B. Nardelli, M. Calandra, R. Car, C. Cavazzoni, D. Ceresoli, M. Cococcioni, N. Colonna, I. Carnimeo, A. D. Corso, S. de Gironcoli, P. Delugas, R. A. D. Jr, A. Ferretti, A. Floris, G. Fratesi, G. Fugallo, R. Gebauer, U. Gerstmann, F. Giustino, T. Gorni, J. Jia, M. Kawamura, H.-Y. Ko, A. Kokalj, E. Küçükbenli, M. Lazzeri, M. Marsili, N. Marzari, F. Mauri, N. L. Nguyen, H.-V. Nguyen, A. O. de-la Roza, L. Paulatto, S. Poncé, D. Rocca, R. Sabatini, B. Santra, M. Schlipf, A. P. Seitsonen, A. Smogunov, I. Timrov, T. Thonhauser, P. Umari, N. Vast, X. Wu, and S. Baroni. Advanced capabilities for materials modelling with quantum espresso. *J. Phys-Condens. Mat.*, 29(46):465901, 2017.
15. P. Giannozzi, S. Baroni, N. Bonini, M. Calandra, R. Car, C. Cavazzoni, D. Ceresoli, G. L. Chiarotti, M. Cococcioni, I. Dabo, A. D. Corso, S. de Gironcoli, S. Fabris, G. Fratesi, R. Gebauer, U. Gerstmann, C. Gougoussis, A. Kokalj, M. Lazzeri, L. Martin-Samos, N. Marzari, F. Mauri, R. Mazzarello, S. Paolini, A. Pasquarello, L. Paulatto, C. Sbraccia, S. Scandolo, G. Sclauzero, A. P. Seitsonen, A. Smogunov, P. Umari, and R. M. Wentzcovitch. Quantum espresso: a modular and open-source software project for quantum simulations of materials. *J. Phys-Condens. Mat.*, 21:395502, 2009.
16. N. Giovambattista, P. J. Rossky, and P. G. Debenedetti. Phase transitions induced by nanoconfinement in liquid water. *Phys. Rev. Lett.*, 102:050603, 2009.
17. E. González Solveyra, E. de la Llave, D. A. Scherlis, and V. Molinero. Melting and crystallization of ice in partially filled nanopores. *J. Phys. Chem. B*, 115(48):14196–14204, 2011.
18. S. Grimme. *J. Comput. Chem.*, 27:1787, 2006.

- 
19. A. B. Grommet, M. Feller, and R. Klajn. Chemical reactivity under nanoconfinement. *Nat. Nanotechnol.*, 15:256–271, 2020.
  20. B. Grunberg, T. Emmmler, E. Gedat, I. Shenderovich, G. Findenegg, H.-H. Limbach, and G. Buntkowsky. Hydrogen bonding of water confined in mesoporous silica mcm-41 and sba-15 studied by 1h solid-state nmr. *Chem.-Eur. J.*, 10:5689–5696, 2004.
  21. Y. Hashikawa, S. Hasegawa, and Y. Murata. A single but hydrogen-bonded water molecule confined in an anisotropic subnanospace. *Chem. Commun.*, 54:13686–13689, 2018.
  22. A. Hassanali, F. Giberti, J. Cuny, T. D. Kühne, and M. Parrinello. Proton transfer through the water gossamer. *P. Natl. Acad. Sci. USA*, page 13723, 2013.
  23. G. Hummer, J. C. Rasaiah, and J. P. Noworyta. Water conduction through the hydrophobic channel of a carbon nanotube. *Nature*, 414(6860):188, 2001.
  24. S. Jahnert, F. Vaca Chavez, G. E. Schaumann, A. Schreiber, M. Schonhoff, and G. H. Findenegg. Melting and freezing of water in cylindrical silica nanopores. *Phys. Chem. Chem. Phys.*, 10:6039–6051, 2008.
  25. J. Kästner and W. Thiel. Bridging the gap between thermodynamic integration and umbrella sampling provides a novel analysis method: “umbrella integration”. *J. Chem. Phys.*, 123(14):144104, 2005.
  26. S. Kittaka, S. Ishimaru, M. Kuranishi, T. Matsuda, and T. Yamaguchi. Enthalpy and interfacial free energy changes of water capillary condensed in mesoporous silica, mcm-41 and sba-15. *Phys. Chem. Chem. Phys.*, 8:3223–3231, 2006.
  27. N. M. A. Krishnan, B. Wang, G. Falzone, Y. Le Pape, N. Neithalath, L. Pilon, M. Bauchy, and G. Sant. Confined water in layered silicates: The origin of anomalous thermal expansion behavior in calcium-silicate-hydrates. *ACS Appl. Mater. Inter.*, 8(51):35621–35627, 2016.
  28. A. Küchler, M. Yoshimoto, S. Luginbühl, F. Mavelli, and P. Walde. Enzymatic reactions in confined environments. *Nat. Nanotechnol.*, 11:409–420, 2016.
  29. S. Kumar, J. M. Rosenberg, D. Bouzida, R. H. Swendsen, and P. A. Kollman. The weighted histogram analysis method for free-energy calculations on biomolecules. I. The method. *J. Comput. Chem.*, 13:1011–1021, 1992.
  30. O. F. Lange and H. Grubmüller. Generalized correlation for biomolecular dynamics. *Proteins*, 62:1053–1061, 2006.
  31. C. Lee, W. Yang, and R. G. Parr. *Phys. Rev. B*, 37:785, 1988.
  32. J. K. Lee, D. Samanta, H. G. Nam, and R. N. Zare. Micrometer-sized water droplets induce spontaneous reduction. *J. Am. Chem. Soc.*, 141:10585–10589, 2019.
  33. X. Liu, X. Lu, R. Wang, E. J. Meijer, and H. Zhou. Acidities of confined water in interlayer space of clay minerals. *GEOCHIM COSMOCHIM AC*, 75:4978–4986, 2011.
  34. E. Mamontov, D. J. Wesolowski, L. Vlcek, P. T. Cummings, J. Rosenqvist, W. Wang, and D. R. Cole. Dynamics of hydration water on rutile studied by backscattering neutron spectroscopy and molecular dynamics simulation. *J. Phys. Chem. C*, 112(32):12334–12341, 2008.

35. Y. Maniwa, K. Matsuda, H. Kyakuno, S. Ogasawara, T. Hibi, H. Kadowaki, S. Suzuki, Y. Achiba, and H. Kataura. Water-filled single-wall carbon nanotubes as molecular nanovalves. *Nat. Mater.*, 6(2):135, 2007.
36. F. Mikami, K. Matsuda, H. Kataura, and Y. Maniwa. Dielectric properties of water inside single-walled carbon nanotubes. *ACS Nano*, 3(5):1279–1287, 2009.
37. S. Mondal and B. Bagchi. Water in carbon nanotubes: Pronounced anisotropy in dielectric dispersion and its microscopic origin. *J. Phys. Chem. Lett.*, 10(20):6287–6292, 2019.
38. E. B. Moore, E. de la Llave, K. Welke, D. A. Scherlis, and V. Molinero. Freezing, melting and structure of ice in a hydrophilic nanopore. *Phys. Chem. Chem. Phys.*, 12:4124–4134, 2010.
39. M. Moqadam, A. Lervik, E. Riccardi, V. Venkatraman, B. K. Alsberg, and T. S. van Erp. Local initiation conditions for water autoionization. *P. Natl. Acad. Sci. USA*, 115(20):E4569–E4576, 2018.
40. D. Muñoz-Santiburcio and D. Marx. Nanoconfinement in slit pores enhances water self-dissociation. *Phys. Rev. Lett.*, 119(5):056002, 2017.
41. C. F. A. Negre, U. N. Morzan, H. P. Hendrickson, R. Pal, G. P. Lisi, J. P. Loria, I. Rivalta, J. Ho, and V. S. Batista. Eigenvector centrality for characterization of protein allosteric pathways. *Proc. Natl. Acad. Sci. U.S.A.*, 115(52):E12201–E12208, 2018.
42. C. Pérez, M. T. Muckle, D. P. Zaleski, N. A. Seifert, B. Temelso, G. C. Shields, Z. Kisiel, and B. H. Pate. Structures of cage, prism, and book isomers of water hexamer from broadband rotational spectroscopy. *Science*, 336(6083):897–901, 2012.
43. T. J. Pinnavaia. Intercalated clay catalysts. *Science*, 220:365–371, 1983.
44. J. O. Richardson, C. Pérez, S. Lobsiger, A. A. Reid, B. Temelso, G. C. Shields, Z. Kisiel, D. J. Wales, B. H. Pate, and S. C. Althorpe. Concerted hydrogen-bond breaking by quantum tunneling in the water hexamer prism. *Science*, 351(6279):1310–1313, 2016.
45. I. Rivalta, M. M. Sultan, N.-S. Lee, G. A. Manley, J. P. Loria, and V. S. Batista. Allosteric pathways in imidazole glycerol phosphate synthase. *Proc. Natl. Acad. Sci. U.S.A.*, 109(22):E1428–E1436, 2012.
46. L. Rubinovich and M. Polak. The intrinsic role of nanoconfinement in chemical equilibrium: Evidence from dna hybridization. *Nano Letters*, 13(5):2247–2251, 2013.
47. M. Sattig and M. Vogel. Dynamic crossovers and stepwise solidification of confined water: A 2h nmr study. *J. Phys. Chem. Lett.*, 5(1):174–178, 2014.
48. A. Schlaich, E. W. Knapp, and R. R. Netz. Water dielectric effects in planar confinement. *Phys. Rev. Lett.*, 117:048001, 2016.
49. A. Schreiber, I. Ketelsen, and G. H. Findenegg. Melting and freezing of water in ordered mesoporous silica materials. *Phys. Chem. Chem. Phys.*, 3:1185–1195, 2001.



- 
50. Y. A. P. Sirkin, A. Hassanali, and D. A. Scherlis. One-dimensional confinement inhibits water dissociation in carbon nanotubes. *J. Phys. Chem. Lett.*, 9(17):5029–5033, 2018.
  51. E. G. Solveyra, E. de la Llave, G. J. A. A. Soler-Illia, V. Molinero, and D. A. Scherlis. Structure, dynamics, and phase behavior of water in tio2 nanopores. *J. Phys. Chem. C*, 117(7):3330–3342, 2013.
  52. M. Sprik. Computation of the pk of liquid water using coordination constraints. *Chem. Phys.*, 258(2):139 – 150, 2000.
  53. M. Sprik. Computation of the pk of liquid water using coordination constraints. *Chem. Phys.*, 258(2):139 – 150, 2000.
  54. W. Stroberg and S. Schnell. Do cellular condensates accelerate biochemical reactions? lessons from microdroplet chemistry. *Biophys. J.*, 115:3–8, 2018.
  55. D. Takaiwa, I. Hatano, K. Koga, and H. Tanaka. Phase diagram of water in carbon nanotubes. *P. Natl. Acad. Sci. USA*, 105(1):39–43, 2008.
  56. G. Torrie and J. P. Valleau. Nonphysical sampling distributions in monte carlo free-energy estimation: Umbrella sampling. *J. Comput. Phys.*, 23:187, 1977.
  57. B. L. Trout and M. Parrinello. The dissociation mechanism of h<sub>2</sub>o in water studied by first-principles molecular dynamics. *Chem. Phys. Lett.*, 288:343–347, 1998.
  58. A. Tuladhar, S. Dewan, S. Pezzotti, F. Brigiano, F. Creazzo, M.-P. Gaigeot, and E. Borguet. Ions tune interfacial water structure and modulate hydrophobic interactions at silica surfaces. *J. Am. Chem. Soc.*, 142(15):6991–7000, 2020.
  59. D. Vanderbilt. Soft self-consistent pseudopotentials in a generalized eigenvalue formalism. *Phys. Rev. B*, 41:7892–7895, 1990.
  60. M. I. Velasco, M. B. Franzoni, E. A. Franceschini, E. Gonzalez Solveyra, D. Scherlis, R. H. Acosta, and G. J. A. A. Soler-Illia. Water confined in mesoporous tio2 aerosols: Insights from nmr experiments and molecular dynamics simulations. *J. Phys. Chem. C*, 121(13):7533–7541, 2017.
  61. Z. Wei, Y. Li, R. G. Cooks, and X. Yan. Accelerated reaction kinetics in microdroplets: Overview and recent developments. *Annual Review of Physical Chemistry*, 71:31–51, 2020.
  62. S. Xu, G. W. Scherer, T. S. Mahadevan, and S. H. Garofalini. Thermal expansion of confined water. *Langmuir*, 25(9):5076–5083, 2009.
  63. X. Yan, R. M. Bain, and R. G. Cooks. Organic reactions in microdroplets: Reaction acceleration revealed by mass spectrometry. *Angew. Chem. Int. Ed.*, 55:2–15, 2016.
  64. T. Zelovich and M. E. Tuckerman. Water layering affects hydroxide diffusion in functionalized nanoconfined environments. *J. Phys. Chem. Lett.*, 11(13):5087–5091, 2020.
  65. J. Zhong, M. Kumar, J. S. Francisco, and X. C. Zeng. Insight into chemistry on cloud/aerosol water surfaces. *Acc. Chem. Res.*, 51(5):1229–1237, 2018.